Reaction Chemistry & Engineering

ROYAL SOCIETY OF CHEMISTRY

PAPER

View Article Online
View Journal | View Issue

Check for updates

Cite this: *React. Chem. Eng.*, 2020, **5**, 685

High redox performance of $Y_{0.5}Ba_{0.5}CoO_{3-\delta}$ for thermochemical oxygen production and separation†

M. Ezbiri,[a] A. Reinhart,[a] B. Huber,[a] K. M. Allen,[b] A. Steinfeld,[a] B. Bulfin *[a] and R. Michalsky *[a]

Received 7th November 2019,
Accepted 13th December 2019

DOI: 10.1039/c9re00430k

rsc.li/reaction-engineering

The efficient production and separation of oxygen is essential for numerous energy-intensive industrial applications in the fuel and mineral processing sectors. A thermochemical redox cycle is considered for separating oxygen from atmospheric air and other gas mixtures using solar or waste process heat. Based on electronic structure (DFT) computations $Y_{0.5}Ba_{0.5}CoO_{3-\delta}$ is selected as a redox material, which surpasses the redox performance of state-of-the-art Cu_2O. The thermochemical oxygen production is experimentally demonstrated by applying a temperature/pressure swing between 573 K at 0.2 bar O_2 and 873 K at 1 bar O_2. An energy balance shows the feasibility of using process waste heat from the solar thermochemical CO_2/H_2O splitting cycle and the potential to compete *vis-a-vis* with cryogenic distillation. Exploratory runs with a packed-bed reactor indicate the potential of both thermochemical oxygen production and separation for scale-up and industrial implementation.

1. Introduction

Oxygen generation/removal is required for fuel and mineral processing and is mainly carried out by cryogenic distillation.[1–4] Other oxygen separation techniques include pressure swing adsorption using zeolites and carbon molecular sieves, and electrochemical separation using mixed ionic-electronic conducting membranes.[1–5] These separation technologies require an electrical input between 100 and 350 kWh per metric ton of O_2.[2–6]

An interesting alternative route to oxygen separation can be achieved *via* a thermochemical process, using a metal oxide redox cycle.[7–9] Heat can be used to drive the reduction of a metal oxide releasing oxygen. The reduced metal oxide can then absorb oxygen from a gas stream such as air. BOC Linde developed such a process, with a temperature and pressure swing thermochemical redox cycle suppling oxygen to an oxy-combustion process.[10] This idea has been further developed in recent years, in particular in the search for new materials. For example, Cu_2O/CuO,[7,11] Mn_3O_4/Mn_2O_3,[11] CoO/Co_3O_4 (ref. 11) and ABO_3-type perovskites,[8,12,13] have all been explored as redox pairs for oxygen separation and production processes.

Perovskites in particular appear to be very promising for this application, as they can exhibit rapid kinetics at relatively low temperatures,[9] and the thermodynamics can be tuned to optimize the energetics of the process.[13] The perovskite $SrFeO_3$, and doped variants, can be considered the state of the art.[9,10] However, cobalt based perovskites such as $SrCoO_3$ appear to be more promising for lower temperature application, and they have the lowest energetic requirement in terms of the enthalpy change of the reduction reaction.[8,13–15]

In this paper, we consider both thermochemical oxygen separation (TOS) and thermochemical oxygen production (TOP) *via* redox cycles with a focus on perovskites with cobalt as the active redox ion. We apply electronic structure calculations on candidate redox materials and select $La_{0.5}Ba_{0.5}CoO_{3-\delta}$, $Pr_{0.5}Ba_{0.5}CoO_{3-\delta}$ and $Y_{0.5}Ba_{0.5}CoO_{3-\delta}$ for further experimental investigation of their O_2 exchange capacity. We performed a comprehensive energy balance to show that the perovskite $Y_{0.5}Ba_{0.5}CoO_{3-\delta}$ can be applied in TOS driven by solar or waste heat and compare the results to the state-of-the-art cryogenic distillation. We also consider the combination of this process with the solar-driven splitting of CO_2 and H_2O, which commonly uses an inert gas for the removal of oxygen.[16–19] TOS can be used to recycle the inert gas, and waste heat from the solar fuel production can be integrated into the TOS processes. Furthermore, we conduct exploratory runs with a packed-bed reactor to elucidate the potential for scale-up and industrial implementation.

[a] *Department of Mechanical and Process Engineering, ETH Zürich, 8092 Zürich, Switzerland. E-mail: bulfinb@ethz.ch, michalskyr@ethz.ch*
[b] *Solar Technology Laboratory, Paul Scherrer Institute, 5232 Villigen, Switzerland*
† Electronic supplementary information (ESI) available. See DOI: 10.1039/c9re00430k

The TOS/TOP approach *via* 2-step redox reactions can be described by eqn (1a) and (1b) for generic perovskite with ABO_3 stoichiometry, where A and B are metal cations in twelve- and six-coordinated interstices, δ is the oxygen nonstoichiometry and $\Delta\delta$ is the oxygen exchange capacity ($\Delta\delta = \delta_{red} - \delta_{ox}$):

Oxidation:

$$ABO_{3-\delta_{red}} + \frac{\Delta\delta}{2}O_2(g) \rightarrow ABO_{3-\delta_{ox}} \quad (1a)$$

Reduction:

$$ABO_{3-\delta_{ox}} \rightarrow ABO_{3-\delta_{red}} + \frac{\Delta\delta}{2}O_2(g) \quad (1b)$$

The redox cycle is performed by applying a temperature/pressure swing. During the oxidation step, oxygen is separated from a gas mixture through the oxidation of the perovskite at low pO_2 and low temperatures. During the reduction step, the perovskite is reduced using a gas mixture at high pO_2 and high temperatures. Redox conditions used in this study for both TOS and TOP are illustrated in Table 7.

2. Computational and experimental section

Electronic structure calculations

The grid-based projector-augmented wave (GPAW) code was employed for density functional theory (DFT) computations.[19,20] Atomic configurations were handled in the atomic simulation environment (ASE),[21] with exchange–correlation interactions treated by the revised Perdew–Burke–Ernzerhof (RPBE) functional.[22] The optimizations of the atomic geometries were executed using the linesearch Broyden–Fletcher–Goldfarb–Shanno (BFGS) algorithm until the maximum force was less than 0.05 eV Å^{-1}. Convergence was achieved using a Fermi–Dirac smearing of 0.1 eV. The results were extrapolated to 0 K. The generalized gradient approximation (GGA) without a Hubbard U correction was used for all DFT calculations, in accordance to previous publications[23–25] AA'BO_3-type perovskites were modeled with $A_2B_2O_6$ models containing a cubic ABO_3 unit cell, with one metal (Ba, Pr, La and Y) at the twelve-coordinated A-site interstices and one metal (Co) at the six-coordinated B-site interstices. All atoms of the bulk models were allowed to optimize their positions (relax). The Brillouin zone of these bulk models having periodic boundary conditions in all directions was sampled with 4 × 4 × 4 k-points. All compositions were treated using spin-polarized calculations. The computed lattice constants are within ±1.6–2.6% of experimental values. The perovskite surfaces were modeled using the (010) facet with AO-termination, which is geometrically symmetric with the (001) and (100) facets dependent on composition, *i.e.* the thermodynamically most stable surface.[26] The surface models contained the same number of atoms as the bulk models, *i.e.* stoichiometry $A_2B_2O_6$, of which the upper ABO_3 layer parallel to the surface was allowed to relax, while the lower layer was constrained to the bulk geometry. All surface structures were periodically repeated parallel to the surface, used 10 Å of vacuum perpendicular to the surface, and employed a k-point sampling of 4 × 4 × 1. To model reduced perovskite surfaces, one third of the stoichiometric lattice oxygen was removed from the upper surface layer, resulting in $A_2B_2O_5$ models corresponding to $\delta = 0.5$.

The Gibbs free energy change of oxygen vacancy formation ($\Delta G_V[O]$) was computed by:[26]

$$\Delta G_V[O] = G_V - (G_S - G_O^r) \quad (2)$$

where G_V and G_S being the Gibbs free energies of formation of the perovskite surfaces with and without oxygen vacancies, respectively, while G_O^r is the reference free energy of the liberated lattice oxygen taken as the energy difference of stable H_2O and H_2 in the gas phase. Negative free energies correspond to exergonic reactions. In this work, the standard partial molar enthalpy change of the metal oxide bulk reduction at 298 K and 1 bar total pressure, $\Delta\bar{h}_{O_2}^{o*}$ is the

Table 1 Structural properties calculated from Rietveld analysis of XRD patterns of LBCO, PBCO and YBCO

	Space group	wt% perovskite (–)	Volume (Å^3)
LBCO	$Pm\bar{3}m$[32]	100	58.9
PBCO	$P4/mmm$[33]	99.1	115.8
YBCO	$P4/mmm$[34]	98.0	112.3

Table 2 Performance indicators of LBCO, PBCO and YBCO based on the TGA experiments shown with Fig. 2

	$T_{red,start}$ (K)	Red. slope (μmol K^{-1})	Reox. slope (μmol$_O$ K^{-1})	$\delta_{end,reox}$ (mol$_O$ mol$_{ABO_3}^{-1}$)	$T_{net,eq}$ (K)
LBCO	692	396	409	0.034	811
PBCO	530	313	373	0.055	725
YBCO	582	541	565	0.035	633

Table 3 Energy requirement per mol of O_2 removed from a 0.5%, 1% and 5% O_2–Ar mixture coming from a solar reactor at 1273 K. In case of no heat recuperation, Δh_{cycle} is calculated *via* $\Delta h_{ha} + \Delta h_{red} + \Delta h_{hs}$, while $\Delta h_{cycl} = \Delta h_{ha} + \Delta h_{red} + \Delta h_{hs} - \left(\frac{\Delta h_{ca} + \Delta h_{cg} + \Delta h_{ox}}{1.25} + \frac{\Delta h_{cs}}{2}\right)$ is used in case of 50% solid and 80% gas heat recuperation

pO_2 (bar)	%-Fraction of heat recovered (–) From solids	From gas	Δh_{cycle} (kJ mol$_{O_2}^{-1}$)	Δh_{avail} (kJ mol$_{O_2}^{-1}$)
0.005	0	0	828	1480
0.005	50	80	−107	1480
0.01	0	0	1280	1483
0.01	50	80	91	1483
0.05	0	0	4217	1507
0.05	50	80	1371	1507

Table 4 Oxygen storage properties of YBCO compared to other state of the art materials in the literature. All data is from TGA analysis

Material	$T_{low} - T_{high}$ [K]	ΔT [bar]	$p_{low} - p_{high}$ [bar]	$\Delta\delta$ [–]
YBCO	563–773	210	0.01–0.2	0.064
$SrFeO_3$ (ref. 9)	623–823	200	0.01–0.2	0.035
$SrCoO_3$ ESI	600–900	300	0.01–0.2	0.029
Cu_2O (ref. 7)	1120–1450	330	0.01–0.01	0.4

Table 5 Extracted $\Delta\delta$ from PBR experiments at 523 K, 563 K, 603 K and 643 K and 0.01 bar pO_2 during oxidation and at 773 K and 0.2 bar pO_2 during reduction

Oxidation temperature (K)	Experimental oxidation period (min)	$\Delta\delta$ ($mol_O\ mol_{ABO_3}^{-1}$)
523	225	0.083
563	175	0.064
603	130	0.043
643	100	0.020

descriptor for the standard partial molar Gibbs free energy change of the metal oxide bulk reduction and oxidation, $\Delta\bar{g}_O^{o*}$ and $-\Delta\bar{g}_{O_2}^{o*}$, respectively. Tabulated thermochemical data,[27] available for a limited number of mostly stoichiometric metal oxides, was used to compute $\Delta\bar{h}_{O_2}^{o*}$, based on previously reported scaling relations between $\Delta\bar{h}_{O_2}^{o*}$ and $\Delta G_V[O]$.[26] The linear scaling relation utilized in this work is:

$$\Delta G_V[O] = 4.49069 \times 10^{-3} \frac{\text{eV}}{\text{kJ mol}_{O_2}^{-1}} \Delta\bar{h}_{O_2}^{o*} - 8.16401 \times 10^{-1}\ \text{eV} \quad (3)$$

In this study, all thermodynamic properties are defined per mole of diatomic oxygen. Details on how the DFT-computed electronic energies were converted into Gibbs free energies at different temperatures and pO_2, the reference energies, and details on the scaling relation[26] are given in ESI.†

Perovskite synthesis – perovskites were synthesized with a modified Pechini method, employing stoichiometric amounts of $La(NO_3)_3{\cdot}H_2O$ (Sigma Aldrich, 99.999%), $Ba(NO_3)_2$ (Alfa Aesar, 99%), $Co(NO_3)_2{\cdot}6\ H_2O$ (Sigma-Aldrich, ≥98%), $Y(NO_3)_3{\cdot}6\ H_2O$ (Aldrich Chemistry, 99.8%), $Pr(NO_3)_3{\cdot}6\ H_2O$ (Aldrich Chemistry, 99.9%), C_2H_6O (Alcosuisse, >96.1% vol) and $C_6H_8O_7$ (Fluka Chemika, ≥99.5%). For the pellet production of $La_{0.5}Ba_{0.5}CoO_{3-\delta}$ (LBCO), $Pr_{0.5}Ba_{0.5}CoO_{3-\delta}$ (PBCO) and $Y_{0.5}Ba_{0.5}CoO_{3-\delta}$ (YBCO), the solid products were ground using mortar and pestle, calcined at 1273 K in air for 5 hours using 5 K min^{-1} for heating and cooling and uniaxially pressed into pellets (5 metric tons, 8 mm in diameter). Granules of YBCO were manufactured by mixing the calcined powder with deflocculant agent (Dolapix CE 64, Zimmer & Schwartz) and deionized water. Granules (around 3 mm in diameter) of the resultant slurry were then pressed out of a syringe onto a platinum sheet and dried. LBCO and PBCO pellets were sintered in air at 1473 K for 5 h, while YBCO pellets, granules and calcined powder were sintered at 1323 K for 24 h. For all materials, a heating and cooling rate of 1 K min^{-1} was employed.

Table 7 Redox conditions of oxygen separation (TOS) and production (TOP) in comparison to state-of-the-art cryogenic distillation

	TOS	TOP
$pO_{2,red,in}$ (bar)	0.2	1
$pO_{2,red,out}$ (bar)	0.4	1
$pO_{2,ox,in}$ (bar)	0.01	0.2
$pO_{2,ox,out}$ (bar)	0.001	0.00035
T_{red} (K)	773	873
T_{ox} (K)	563	573
$\Delta\delta$ ($mol_O\ mol_{ABO_3}^{-1}$)	0.064	0.114
Δh_{req} (kJ $mol_{O_2}^{-1}$)	0	377
State-of-the-art	Cryogenics	Cryogenics
E_{th}	50 kJ $mol_{N_2}^{-1}$ (ref. 6)	78 kJ $mol_{O_2}^{-1}$ (ref. 6)

Solid-state analysis

Room-temperature X-ray diffraction (XRD) on YBCO, PBCO and LBCO and high-temperature XRD (HT-XRD) on YBCO were performed in the Bragg Brentano geometry using Cu Kα radiation (20–80° 2θ, 0.01° min^{-1} scan rate, 45 kV/20 mA output, PANalytical/X'Pert MPD/DY636, Philips). HT-XRD scans were executed between 308 and 923 K in 0.2 bar O_2 in N_2 during heating up and 0.01 bar O_2 in Ar during cooling down using a platinum sheet as sample holder. Basic structural data of the room temperature measurement was obtained by multiphase Rietveld analysis (Jana2006). The morphology of pellets and granules was analyzed *via*

Table 6 Energy balance of TOP in comparison to state-of-the-art cryogenic distillation. E_{el} and E_{th} denote the electrical and thermal energies, respectively, while Δh_{req} and Δh_{recup} denote the required energy and the energy recuperated by solid and gas heat recuperation, respectively

TOP				
%-Fraction of heat recovered (–)				
From solids	From gas	Δh_{req} (kJ $mol_{O_2}^{-1}$)	Δh_{recup} (kJ $mol_{O_2}^{-1}$)	Δh_{cycle} (kJ $mol_{O_2}^{-1}$)
50	80	844	466	377
Cryogenic distillation				
Purity	E_{el} (kJ $mol_{O_2}^{-1}$)	E_{th} (kJ $mol_{O_2}^{-1}$)		
99.5%	31	78		

scanning electron microscopy (SEM; HITACHI Tabletop Microscope TM-1000). Brunauer–Emmett Teller (BET, Micrometrics TriStar 3000 N_2 absorption analyzer) measurements were performed to acquire information about the specific surface area of the YBCO granules. The BET results, XRD patterns and SEM images are presented in ESI.†

Screening

PBCO, LBCO and YBCO were screened using thermogravimetric analysis (TGA) between 303 and 1273 K using +2 and −2 K min^{-1} in 0.2 bar O_2 in N_2 during heating and in 0.005 bar O_2 in Ar during cooling. The slow heating and cooling rates were chosen to ensure thermodynamic equilibrium at all times. To correct for buoyancy, blank runs were performed using the same measurement conditions employed for the experimental runs.

Thermodynamic analysis

The thermodynamic analysis was performed to extract the reduction enthalpy, Δh_{red}, using the approach of Scheffe *et al.*:[28] Oxygen release and uptake of a perovskite can generally be described as:

$$ABO_3 \leftrightarrow ABO_{3-\delta} + \frac{\delta}{2}O_2(g) \tag{4}$$

From eqn (4) we can derive the oxygen partial pressure dependence (pO_2) on the equilibrium constant K:

$$K = (pO_2)^{0.5} \tag{5}$$

and its relation to the standard Gibbs free energy change ($\Delta\bar{g}^\circ_{O_2}$):

$$\Delta\bar{g}^\circ_{O_2}(\delta, T) = -2RT\ln K = -RT\ln(pO_2/p^\circ) \tag{6}$$

where p° is the standard pressure at 1 bar. $\Delta g^\circ_{O_2}$ can further be derived from the standard partial molar enthalpy change of reduction, $\Delta\bar{h}^\circ_{O_2}$, and the standard partial molar entropy change of reduction, $\Delta\bar{s}^\circ_{O_2}$:

$$\Delta\bar{g}^\circ_{O_2}(\delta, T) = \Delta\bar{h}^\circ_{O_2}(\delta) - T\Delta\bar{s}^\circ_{O_2}(\delta) \tag{7}$$

Combining eqn (6) and (7), we obtain $\Delta\bar{h}^\circ_{O_2}$ and $\Delta\bar{s}^\circ_{O_2}$ as a function of δ by determining the slope and intercept of $-\ln(pO_2/p^\circ)$ as a function of T^{-1} for a constant δ (*cf.* eqn (8)):

$$-\ln\left(\frac{pO_2}{p^\circ}\right) = \frac{\Delta\bar{h}^\circ_{O_2}(\delta)}{RT} - \frac{\Delta\bar{s}^\circ_{O_2}(\delta)}{R}\bigg|_{\delta=\text{const.}} \tag{8}$$

Finally, integrating $\Delta\bar{h}^\circ_{O_2}$ over the initial and final δ, we obtain the reduction enthalpy, Δh_{red} (*cf.* eqn (9)). Δh_{red} is directly related to the solar input required to drive the redox reaction.

$$\Delta h_{red} = \frac{\int_{\delta_i}^{\delta_f}\Delta\bar{h}^\circ_{O_2}(\delta)}{\delta_f - \delta_i}\mathrm{d}\delta \tag{9}$$

where δ_i and δ_f are the oxygen nonstoichiometries before and after reduction, respectively.

To determine Δh_{red}, TGA measurements were conducted by heating up to 1073 K in 0.2 bar O_2 in N_2 and cooling down in 0.005, 0.01, 0.05 and 0.2 bar O_2 in Ar, using slow rates of +2 K min^{-1} and −2 K min^{-1} to ensure thermodynamic equilibrium at all times (*cf.* Fig. 2).

Molar heat capacity measurements

The molar heat capacity (c_p) of YBCO was measured with a heat flux differential scanning calorimetry (DSC, SENSYS evo DSC, Setaram). The sample, in the form of crushed pellet pieces with a total weight of 178.5 mg, was subjected to an Ar flow (99.998%, Carbagas) of 5 mL min^{-1} between 373 and 1073 K using a heating rate of +10 K min^{-1}. To evaluate the measurement accuracy, we further acquired the c_p of CeO_2 and compared the result to previously published data[29] (*cf.* Fig. S11†), revealing a discrepancy on average of only 1.94%. All experimental curves were fitted using the least-squares fitting method.

Oxygen nonstoichiometry cycling measurements

Oxygen nonstoichiometry (δ) was measured using a thermogravimetric analyzer (TGA, STA 409/C/3, Netzsch). YBCO granules (112 mg) were placed on a platinum crucible supported with an Al_2O_3 rod on the microbalance of the TGA (±0.1 μg). The granules were thereafter exposed to a gas flow (constant flow rate of 200 mL min^{-1}) with specified pO_2 that was adjusted *via* mixing O_2 (99.5%, Messer) and N_2 (99.999%, Carbagas) using three electronic mass flow controllers (MFC, MFC400, Netzsch; accuracy ±1%, precision ±1 mL min^{-1}). For the TOS process, the mass change of the granules was recorded during 38 consecutive redox cycles at 773 K and 0.2

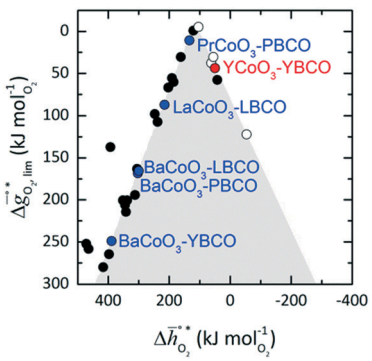

Fig. 1 The limiting Gibbs free energy change of the reduction reaction ($\Delta\bar{g}^{\circ*}_{O_2,\text{lim}}$) as a function of the standard partial molar enthalpy change of the oxide reduction at 298 K ($\Delta\bar{h}^{\circ*}_{O_2}$). All data is at 1 bar. The coloured compositions represent perovskites, with blue marked materials limited by reduction, and red marked materials limited by oxidation. The ABO_3-type perovskite written before the $AA'BO_3$-type perovskite is the surface layer of the $AA'BO_3$-type perovskite. Black and white round symbols represent solid metal oxides and metal/metal oxide pairs limited by their oxide reduction and oxidation, respectively.

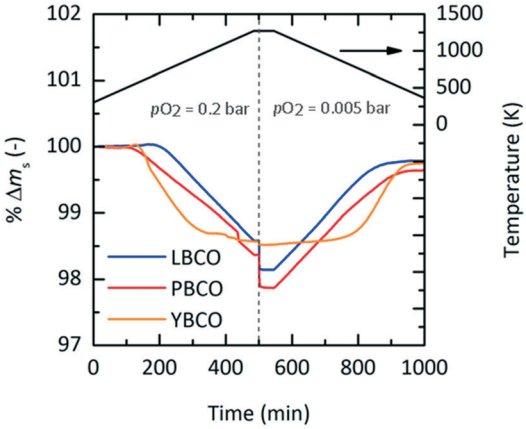

Fig. 2 Percent weight change *vs.* time from 298 to 1273 K, changing from 0.2 bar O_2 to 0.005 bar O_2 at the dashed line for LBCO, PBCO and YBCO. Heating and cooling rates were set to +2 K min^{-1} and −2 K min^{-1}, respectively.

bar O_2 in N_2 for reduction and 563 K and 0.01 bar O_2 in Ar for oxidation using +20 K min^{-1} and −20 K min^{-1}, respectively. For the TOP process, the mass change of the samples was recorded during 50 consecutive redox cycles at 873 K and 1 bar O_2 for reduction and 573 K and pO_2 and 0.2 bar O_2 in N_2 for oxidation using +20 K min^{-1} and −20 K min^{-1}, respectively. To correct for buoyancy, blank runs were performed using the same measurement conditions employed for the experimental runs.

Packed bed reactor experiments

YBCO was tested in a packed bed reactor (PBR) setup, in accordance to previous experimental campaigns investigating gas–solid reactions.[7] PBR experiments for the TOS process were performed with a vertically inserted quartz tube with a diameter of 1 cm in an electric furnace (Carbolite, VS 17/250). Gas flows were introduced from the bottom at 20 mL min^{-1} and controlled using two electronic MFC (EL-Flow Select, Bronkhorst; accuracy ±0.5%). The oxygen concentration in the outlet gas flow was monitored by gas chromatography (GC, Agilent Micro GC, CP-4900). Two K-type thermocouples were inserted in the packed bed. From the bottom to the top, the reactor bed consisted of approximately 2 cm of compressed Al_2O_3 wool, 0.5 cm quartz sand with a diameter of 200–300 μm, 15 cm YBCO powder (8 g) mixed with quartz sand (16 g) and 1 cm pure quartz sand on top. A total of 15 consecutive cycles were executed. Reduction was always performed at 773 K and 0.2 bar O_2 in N_2 and held isothermally for 45 min. 30 min prior to cooling down, 0.2 bar O_2 in N_2 was exchanged to 0.01 bar O_2 to ensure full gas replacement in the PBR. Oxidation was performed in 0.01 bar O_2 at 563 K (cycles 1–4, 240 min isothermal), 523 K (cycles 5–7, 300 min isothermal), 603 K (cycles 8–12, 180 min isothermal) and 643 K (cycles 13–15, 180 min isothermal). 15 min prior to heating up to 773 K, 0.01 bar O_2 in Ar was exchanged to 0.2 bar O_2 in N_2 to ensure full gas replacement.

For the TOP process an Inconel tube with a diameter of 1 cm in an electric furnace (Carbolite, VS 17/250) was employed. Gas flows were introduced from the bottom. Oxidation was performed at 5 mL min^{-1}, 0.2 bar O_2 in N_2 and 573 K during 240 min, while reduction was done at 10 mL min^{-1}, 873 K and 1 bar O_2 during 160 min. 60 and 30 min prior to cooling down from 873 to 573 K and prior to heating up from 573 to 873 K, respectively, respective gases were exchanged to ensure full gas replacement within the PBR. The oxygen concentration and gas flows were monitored by GC (Agilent Micro GC, CP-4900) and two electronic MFCs (EL-Flow Select, Bronkhorst; accuracy ±0.5%), respectively. An additional MFC (F-201CV, Bronkhorst; accuracy ±0.5%) was used to record absolute gas flows at the outlet of the PBR. Two K-type thermocouples were inserted in the packed bed. From the bottom to the top, the reactor bed consisted of approximately 2 cm of compressed Al_2O_3 wool, 0.5 cm quartz sand with a diameter of 200–300 μm, 13 cm YBCO granules (9 g) and 1 cm pure quartz sand on top. A total of 9 consecutive cycles were executed.

3. Results and discussion

Materials design

It was previously shown that metal oxide redox materials can be designed by plotting the limiting partial molar Gibbs free energy, $\Delta\bar{g}^{\circ*}_{O_2,\mathrm{lim}}$ as a function of the descriptor $\Delta\bar{h}^{\circ*}_{O_2}$, *i.e.* the partial molar enthalpy at room temperature.[8,26] The limiting Gibbs free energy $\Delta\bar{g}^{\circ*}_{O_2,\mathrm{lim}}$ is defined as the larger Gibbs free energy change of either the reduction or oxidation reaction at the conditions to be used in the process. In other words, it is Gibbs free energy change of the reaction step, either oxidation or reduction, which is limiting the overall redox process. Here, $\Delta\bar{g}^{\circ*}_{O_2,\mathrm{lim}}$ and $\Delta\bar{h}^{\circ*}_{O_2}$ were computed for 32 solid metal oxides and six metal/metal oxide pairs at 563 K and 0.01 bar O_2 for oxidation and 773 K and 0.2 bar O_2 for reduction. Fig. 1 shows $\Delta\bar{g}^{\circ*}_{O_2,\mathrm{lim}}$ as a function of $\Delta\bar{h}^{\circ*}_{O_2}$ near the intersection of $\Delta\bar{g}^{\circ*}_{O_2,\mathrm{lim}}$. Compounds with balanced, and thus favourable, redox behaviour are located near the top of the resulting volcano-shaped curve, *i.e.* they bind oxygen strongly enough at lower temperatures, but weakly enough to be reduced at moderately higher temperatures. Hence, the separation of oxygen from gas mixtures with a lower pO_2 than the pO_2 during the metal oxide reduction can be characterized by an intermediately strong bonding of the lattice oxygen.[8] Ideally, $\Delta\bar{g}^{\circ*}_{O_2,\mathrm{lim}}$ is exergonic, which is only reached by RhO/Rh_2O and PbO/Pb_3O_4, rare and toxic materials, respectively. Various perovskite compositions, including LBCO, PBCO and YBCO, were therefore computed to tailor inexpensive and non-toxic redox materials (*cf.* Fig. 1), by modelling stoichiometric ABO_3(010) and oxygen-deficient $ABO_{2.5}$(010) with the grid-based projector-augmented wave (GPAW) and atomic simulation environment (ASE) electronic-structure code.[19–21] $\Delta\bar{g}^{\circ*}_{O_2,\mathrm{lim}}$ and $\Delta\bar{h}^{\circ*}_{O_2}$ were then calculated

from the scaling of $\Delta G_V[O]$ and the redox energetics of the bulk oxides (*cf.* ESI†).[8,26,30] The surface layer of each AA'BO_3-type perovskite is ideally composed of either $ACoO_3$ or A'CoO_3. Fig. 1 displays the results of both possibilities, *i.e.* $BaCoO_3$–YBCO denotes that for YBCO, $BaCoO_3$ is on the surface. Interestingly, $YCoO_3$–YBCO is the only composition for which oxidation is the limiting reaction.

To verify the DFT-predicted trends and find a suitable material for thermochemical redox processes, LBCO, PBCO and YBCO were tested experimentally at different sets of redox conditions, presented in the next subsections.

Structural characterization

Fig. S1† displays the XRD spectra of sintered LBCO, PBCO and YBCO which were all identified to be in the perovskite-type structure. While LBCO was determined to be cubic, PBCO and YBCO revealed a tetragonal structure (*cf.* Table 1). From the XRD scans we see that decreasing ionic radii of the A-site dopants ($La^{3+} > Pr^{3+} > Y^{3+}$), result in increasing structural lattice distortions along with a shift towards higher 2θ angles (*cf.* Fig. S1†).[31] Detected impurities originate from BaO in PBCO and from Y_2O_3 and $YBaCo_2O_5$ in YBCO.

Furthermore, the high-temperature XRD (HT-XRD) scans YBCO shown with Fig. S3† illustrate that this compound stays stable throughout the whole temperature range between 308 and 923 K in 0.2 and 0.01 bar O_2 during heating and cooling, respectively.

Experimental screening

To investigate the established redox trends by DFT, TGA experiments were conducted with LBCO, PBCO and YBCO between 303 and 1273 K (*cf.* Fig. 2). A pO_2 of 0.2 bar was chosen during heating, while 0.005 bar O_2 was taken during cooling. Heating and cooling rates were both set to a low value of +2 K min^{-1} and −2 K min^{-1} such that thermodynamic equilibrium at all times can be assumed. We see that the three compositions all reduce and oxidize, with PBCO reaching the largest reduction extent.

To evaluate which of the three materials performs best, several performance indicators based on the experiments shown with Fig. 2 were applied (*cf.* Table 2). $T_{red,start}$ corresponds to the temperature at which the perovskites start to reduce, $\delta_{end,reox}$ corresponds to the final oxygen nonstoichiometry of the reoxidized state and $T_{net,eq}$ corresponds to the temperature that has to be exceeded during reduction to achieve a net $\Delta\delta$ (*cf.* Fig. S6†). The relative oxygen nonstoichiometries can be calculated from the data shown with Fig. 2 with:

$$\Delta\delta = \Delta m_s \frac{M_s}{M_O} \tag{10}$$

where Δm_s is the relative weight loss at equilibrium, and M_s and M_O are the molar mass of the sample and of monoatomic oxygen, respectively. M_s was taken as the molar mass of the fully oxidized perovskite, ABO_3.

In summary, an ideal material for TOS has a low $T_{net,eq}$, resulting from a low $T_{red,start}$ and steep reduction and reoxidation slopes, *i.e.* fast reaction rates. Thus, the results suggest that YBCO is the most promising material from the three tested perovskites, having a $T_{net,eq}$ of only 633 K (*cf.* Table 2).

The following two sections focus on experiments performed for thermochemical oxygen separation and production using YBCO at different sets of redox conditions, summarized in Table 7.

Thermodynamic analysis

In this section, we report the acquisition of $\Delta\bar{h}^{\circ}_{O_2}$ and Δh_{red} (*cf.* eqn (8) and (9)). Δh_{red} is directly related to the energy input required to drive the redox reaction,[28] and is thus crucial to establish an energy balance. Fig. 3a shows the $\Delta\delta$ of YBCO at 0.005 bar O_2, 0.01 bar O_2, 0.05 bar O_2 and 0.2 bar O_2 between 400 and 1073 K. As expected, we see that a higher pO_2 shifts the thermodynamic equilibrium towards higher oxygen nonstoichiometries, *i.e.* lower reduction extents. The relative non-stoichiometry values $\Delta\delta$ can also be seen to converge towards a maximum reduction extent of around $\Delta\delta$ = 0.2 $mol_O\ mol_{ABO_3}^{-1}$, for all oxygen partial pressures.

To explain this maximum $\Delta\delta$, we need to consider the possible reduction pathways of the perovskite. Yttrium will always remain in a 3+ oxidation state, and barium in a 2+ state. The fully oxidised perovskite would then have oxidation states $Y_{0.5}^{3+}$ $Ba_{0.5}^{2+}$ $Co_{0.5}^{3+}$ $Co_{0.5}^{4+}$ O_3^{2-}, which could be considered as a solid solution of the two perovskites $YCoO_3$ and $BaCoO_3$. The formation of oxygen vacancies could then take place by the reduction of Co^{4+} to Co^{3+}, or Co^{3+} to Co^{2+}. DFT calculations of $YCoO_3$ reduction performed by the authors suggest an enthalpy of reduction of $\Delta\bar{h}^{\circ}_{O_2}$.[25] This is much larger than the experimental values measured here (Fig. 3b) and also means that reduction of the perovskite *via* Co^{3+} to Co^{2+}, would require higher temperatures. Indeed, experimental results obtained by Mei *et al.* for the reduction of $LaCoO_{3-\delta}$ *via* Co^{3+} to Co^{2+} transitions show only very small non-stoichiometry of $\delta < 0.001$, for the most reducing

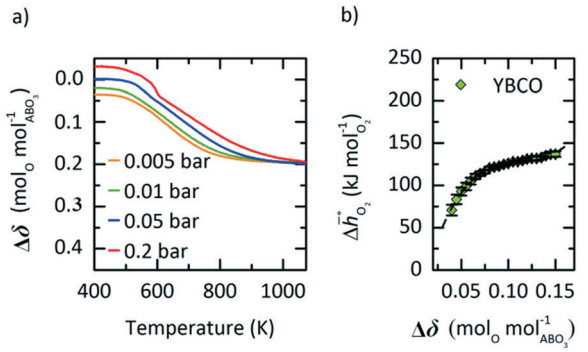

Fig. 3 a) Oxygen nonstoichiometry, δ, *vs.* temperature during reoxidation of YBCO at 0.005, 0.01, 0.05 and 0.2 bar O_2, and b) standard partial molar enthalpy change of reduction, $\Delta\bar{h}^{\circ}_{O_2}$, as a function of δ for YBCO. Error bars are ±2σ confidence intervals of the slope of $-\ln(pO_2/p^{\circ})$ *versus* T^{-1} (*cf.* Fig. S7†).

conditions seen in Fig. 3a) of T = 1073 K and pO_2 = 0.005 bar. On the other hand, reduction *via* Co^{4+} to Co^{3+} occurs readily at low temperatures in $SrCoO_3$,[8] and other perovskites containing Co^{4+}.[14] Additionally, these Co^{4+} perovskites exhibit non-stoicheometry even at ambient conditions when cooled under air, which explains the positive values of $\Delta\delta$ seen in Fig. 3a. It is therefore likely that the majority of the reduction takes place *via* Co^{4+} to Co^{3+} transitions. The value of $\Delta\delta \approx 0.2$ that the nonstoicheometry converges towards could then correspond to complete reduction of Co^{4+} to Co^{3+} giving a reduced perovskite with a stoichiometry of $Y_{0.5}Ba_{0.5}CoO_{2.75}$. This would mean that the zero point in Fig. 3a is $Y_{0.5}Ba_{0.5}CoO_{2.95}$, but as their may be some reduction of Co^{3+}, we cannot with certainty state the exact stoichiometry.

From the data shown with Fig. 3a, S7† and eqn (8), $\Delta\bar{h}^{\circ}_{O_2}$ was deduced (*cf.* Fig. 3b). The good linear fit of the data shown with Fig. S7† ($R^2 > 0.94$) confirms that $\Delta\bar{h}^{\circ}_{O_2}$ does not have strong dependence on temperature at the investigated conditions. Fig. 3b shows increasing $\Delta\bar{h}^{\circ}_{O_2}$ with increasing δ values, as observed by Babiniec *et al.*[35] for $La_xSr_{1-x}Co_yM_{1-y}O_{3-\delta}$ (M = Mn, Fe) and Takacs *et al.*[36] for $La_{0.6}M_{0.4}MnO_{3-\delta}$ (M = Sr, Ca). The data in Fig. 3a may be kinetically limited at lower temperatures (T < 600 K), so that the Van't Hoff method may not be accurate in this region. The steep drop in Fig. 3b at lower $\Delta\delta < 0.07$, may be a result of this. Symbols correspond to the measured δ values shown with Fig. 3, while the dashed line corresponds to a third-degree fit ($R^2 > 0.99$). Error bars are $\pm 2\sigma$ confidence intervals of the slope of $-\ln(pO_2/p^{\circ})$ *versus* T^{-1} (*cf.* Fig. S7†).

Applying eqn (9) to the result shown with Fig. 3b, we obtain a reduction enthalpy change of Δh_{red} = 121 kJ $mol_{O_2}^{-1}$ for YBCO at a $\Delta\delta$ of 0.064 mol_O $mol_{ABO_3}^{-1}$.

Thermochemical oxygen separation

In the following sections we present results for a TOS processes using YBCO, including an energy balance, cycle stability runs in the TGA, and a packed bed reactor demonstration.

Energy balance

Using Δh_{red} and measured c_p (*cf.* Fig. S10†) of YBCO, an energy flow diagram for a redox cycle separating oxygen from a 1% O_2–Ar stream is depicted in Fig. 4. The energy requirement per mole of O_2, Δh_{cycle}, is calculated from the thermodynamic data of YBCO. c_p values of gas mixtures are approximated using the pure component properties obtained from NIST-JANAF tables.[37] Assumed temperature/pressure-swing operating conditions are 773 K and 0.2 bar O_2 for reduction and 563 K and 0.01 bar O_2 for oxidation. The choice of these conditions was made based on the knowledge acquired by the thermodynamic assessment (*cf.* Fig. 3). All involved equations used for the calculations of the different components are shown in ESI.† According to the net energy balance (*cf.* Fig. 4), the required energy to separate O_2 from a 1% O_2–Ar gas stream amounts to 1.82 MJ_{th} $mol_{O_2}^{-1}$, while 1.83 MJ $mol_{O_2}^{-1}$is available in form of sensible heat from gas and solid heat exchange. In the present study, TOS is considered for the cleaning of the outlet stream from a solar reactor, which can be assumed to be at around 1273 K at the currently employed solar reactor conditions with the state-of-the-art material CeO_2.[38] This heat can be directly extracted in the TOS redox cycle using a printed-circuit heat exchanger, achieving an effectiveness of up to 97%.[39] The extractable sensible heat (Δh_{avail}) is considered as the sensible heat of the 1% O_2–Ar gas mixture between 1273 and 563 K and it amounts to 1.48 MJ $mol_{O_2}^{-1}$. In this scenario, no heating of the incoming 1% O_2–Ar gas mixture is necessary (Δh_{hg} = 0) and thus, Δh_{cycle} is 1.28 MJ $mol_{O_2}^{-1}$. Table 3 summarizes the energy requirements, assuming 50% solid and 80% gas heat recuperations and no heat recuperation at all, for O_2–Ar gas mixtures of 0.005, 0.01 and 0.05 bar O_2 coming from a solar reactor at 1273 K. We see from Table 3 that with 0.005 and

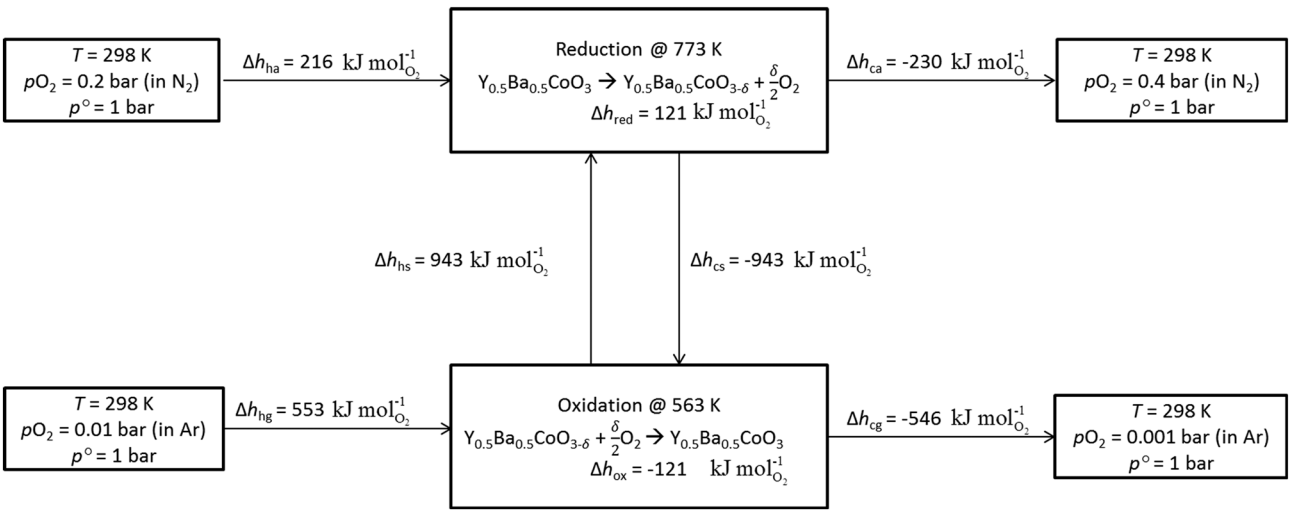

Fig. 4 Energy balance of TOS *via* redox cycle using YBCO at 773 K and 0.2 bar O_2 during reduction and 563 K and 0.01 bar O_2 during oxidation.

0.01 bar O_2, $\Delta h_{avail} > \Delta h_{cycle}$. With 0.05 bar O_2, $\Delta h_{avail} < \Delta h_{cycle}$ when no gas and solid heat recuperation is applied. This is the only tested scenario where an additional energy input would be necessary to run the process. Oxidation at 0.05 bar O_2 is more energy intensive than in case of lower pO_2 values, because of the larger amount of reactive material to be heated. At high pO_2 values, a higher quantity of oxygen has to be separated per redox cycle. This has a significant impact on the energy needed to heat the solid, Δh_{hs}, which increases from 334 and 668 to 3342 kJ $mol_{O_2}^{-1}$ for 0.005 and 0.01 to 0.05 bar O_2, respectively. The larger $\Delta\delta$ at higher pO_2 values, *i.e.* here it increases from 0.053 and 0.064 to 0.090 mol_O $mol_{ABO_3}^{-1}$ upon changing from 0.005 and 0.01 to 0.05 bar O_2, respectively, cannot compensate for the increased Δh_{hs}. Furthermore, the energy needed to heat the air, Δh_{ha}, increases from 77 and 153 to 767 kJ $mol_{O_2}^{-1}$for 0.005 and 0.01 to 0.05 bar O_2, respectively, since the required molar amount of air is roughly half the molar amount of perovskite, according to Hänchen *et al.*[7] Δh_{avail} at 0.05 bar O_2 increases slightly compared to 0.01 and 0.005 bar O_2, because the c_p of O_2 (29.4 J mol K^{-1}) is larger than theone of Ar (20.8 J mol K^{-1}). Summarizing, the energy balance is favored at rather low pO_2 and heat recuperation is essential at high pO_2. However, at low pO_2 oxidation rates are expected to decrease.

Thermochemical cycling experiments for TOS

To verify if YBCO is suitable in an industrial implementation, porous granules were produced according to the procedure described in the experimental section. Production of the granules was much more efficient than pellet production, while still having a diameter large enough to avoid significant channelling effects and pressure drops if employed in a PBR. Fig. 5 shows the $\Delta\delta$ of YBCO granules cycled 38 times in a TGA between 563 K and 0.01 bar O_2 during oxidation and 773 K and 0.2 bar O_2 during reduction. We see that $\Delta\delta$ stays stable throughout all executed cycles, reaching values of around 0.061 mol_O $mol_{ABO_3}^{-1}$. It is assumed that the slightly lower value of 0.061 *vs.* 0.064 mol_O $mol_{ABO_3}^{-1}$, observed with the pellets (*cf.* Fig. 3), might originate from the two additional small XRD peaks around 28° (indexed by *, *cf.* Fig. S2†), which might be due to an ordering of excess oxygen forming a superstructure.[40]

The oxygen storage capacity $\Delta\delta$, of YBCO, looks very good when compared to other materials studied for TOS and TOP processes, as can be seen in Table 4. YBCO has approximately double the oxygen storage capacity of both $SrFeO_3$ and $SrCoO_3$ over similar temperature and pressure ranges. Cu_2O (ref. 7) on the other hand, has a large oxygen storage due to the stoichiometric nature of the reaction, but requires much higher temperatures. It is clear that the low temperature redox conditions employed with YBCO would not work for Cu_2O, since Ezbiri *et al.*[8] previously showed that Cu_2O irreversibly oxidizes to CuO, when cycled between 900 and 600 K at 0.2 and 0.035 bar O_2, respectively. We therefore concluded for applications in the lower temperature range investigated here that YBCO has superior performance compared to the state of the art.

Packed bed reactor experiments for TOS

PBR experiments were executed to test the potential of YBCO for an industrial setting. To minimize the effects of channelling and pressure drops in the PBR, the previously discussed YBCO granules were initially used. However, the available setup did not allow for YBCO granules to reach thermodynamic equilibrium, possibly due to mass transfer limitations in the gas phase and the lower specific area of the granules (*cf.* Fig. S13†). Hence, the results executed with the YBCO powder are shown. Fig. 6 displays the measured pO_2 at the outlet of the PBR along with the temperature and the pO_2 at the inlet of the PBR as a function of time. Fig. 6 shows oxidation at 563 K; Fig. S12† shows oxidation at 523, 603 and 643 K. For all these oxidation temperatures,

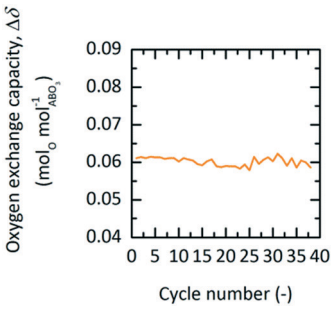

Fig. 5 Oxygen exchange capacity, $\Delta\delta$, *vs.* cycle number of YBCO granules at 0.01 bar O_2 and 563 K during oxidation and 0.2 bar O_2 at 773 K during reduction for TOS.

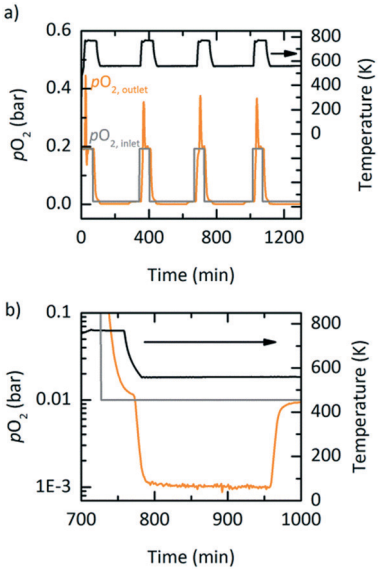

Fig. 6 a) A number of cycles in the PBR showing temperature, pO_2 at the outlet (orange) and pO_2 at the inlet of the PBR (grey) using YBCO at 563 K and 0.01 bar pO_2 for oxidation and 773 K and 0.2 bar pO_2 for reduction. b) A single cycle from a).

thermodynamic equilibrium was reached during oxidation. We see from Fig. 6b that during oxidation, the pO_2 drops from 0.01 bar O_2 to 0.001 bar O_2 over a steady period of 175 minutes, which can clearly be attributed to the reoxidation reaction of YBCO. 0.001 bar O_2 is the maximum allowable O_2 concentration in recycled inert gas.[7] Reaching 955 minutes in Fig. 6b, the pO_2 quickly increases back to 0.01 bar O_2, which means that the whole reactor bed has been oxidized. An amount of 3.13 litres of O_2 is separated during the oxidation at 563 K, in each of the cycles, corresponding to 0.064 mol_O $mol_{ABO_3}^{-1}$ as observed in the TGA (*cf.* Table 5). Table 5 further shows the oxidation time and $\Delta\delta$ of the PBR experiments at oxidation temperatures of 523, 603 and 643 K. As expected, we see that the time until oxidation and the $\Delta\delta$ values increase with decreasing oxidation temperature.

Thermochemical oxygen production

In the following sections we present results for a TOP processes using YBCO, again including an energy balance, cycle stability runs in the TGA, and a packed bed reactor demonstration of the process.

Energy balance

This section presents the energy balance established for TOP, similar to the energy balance illustrated in Fig. 4. Here, a different set of redox conditions is employed (*cf.* Table 7) with 673 K and 0.2 bar O_2 during oxidation and 873 K and 1 bar O_2 during reduction. Since this process is not coupled to another high-temperature technology, Δh_{hg} cannot be taken as zero, *i.e.*

$$\Delta h_{cycl} = \Delta h_{ha} + \Delta h_{red} + \Delta h_{hs} + \Delta h_{hg} - \left(\frac{\Delta h_{ca} + \Delta h_{cg} + \Delta h_{oxi}}{1.25} + \frac{\Delta h_{cs}}{2}\right)$$

assuming 80 and 50% gas and solid heat recuperation, respectively. With YBCO and the employed redox conditions, Δh_{cycle} amounts to 377 kJ $mol_{O_2}^{-1}$, while state-of-the-art cryogenic distillation requires a thermal energy of 78 kJ $mol_{O_2}^{-1}$, assuming a conversion factor of 0.4 (for state-of-the-art coal-fired power plants[41]) between electric (E_{el}) and thermal energy (E_{th}) (*cf.* Table 6). We thus conclude that TOP using YBCO at the used redox conditions might only compete with cryogenic distillation if coupled to another high-temperature technology, such as oxy-fuel combustion,[2,10] where the cryogenic air separation unit is a major economic drawback. Other possible technologies, where the wider use of pure oxygen could reduce CO_2 emissions, include integrated gasification combined cycles and the partial oxidation of methane.[5]

Thermochemical cycling experiments for TOP

Using TGA, 50 redox cycles were performed with YBCO granules at 573 K and 0.2 bar O_2 during oxidation and at 873 K and 1 bar O_2 during reduction. We see that $\Delta\delta$ stays stable at around 0.1 mol_O $mol_{ABO_3}^{-1}$ throughout all executed redox cycles (*cf.* Fig. 7).

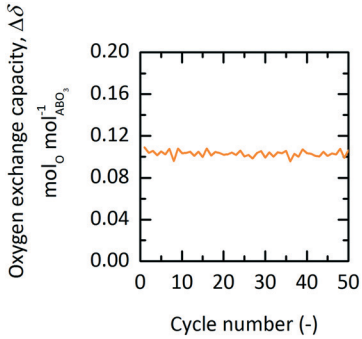

Fig. 7 Oxygen exchange capacity, $\Delta\delta$, *vs.* cycle number of YBCO at 0.2 bar O_2 and 573 K during oxidation and 1 bar O_2 at 873 K during reduction for TOP.

Packed bed reactor experiments for TOP

Exploratory experimental runs with a packed bed reactor were executed using YBCO granules, where in this case the granules were indeed suitable as they did reach thermodynamic equilibrium. This was likely due to the higher temperature operation when compared to TOS. Fig. 8 shows the absolute gas flow and pO_2 measured at the outlet of the reactor *vs.* time for nine consecutive redox cycles. 5 and 10 mL min^{-1} gas flows were used during oxidation and reduction, respectively. The changes in absolute gas flow during oxidation and reduction are a clear indication of the reactivity of YBCO. We further note that the pO_2 does not change during reduction since it is at a 100% at the inlet already. During oxidation, however, a decrease in pO_2 from the set point of 0.2 bar O_2 is observed.

Table 7 gives an overview of the used redox conditions, the resulting $\Delta\delta$ and the required energies of TOS and TOP in comparison to state-of-the-art cryogenic distillation.

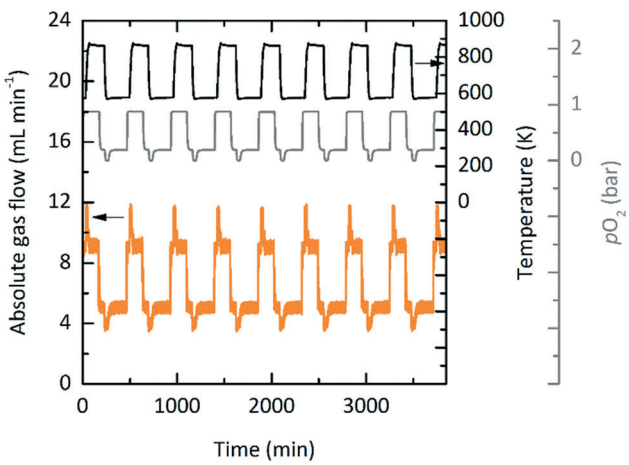

Fig. 8 Consecutive redox cycles for TOP with a packed-bed reactor. Absolute gas flow (orange) and pO_2 (grey) measured at the outlet of the packed bed reactor *vs.* time using YBCO at 573 K and 0.2 bar O_2 during oxidation and 873 K and 1 bar O_2 during reduction. The absolute gas flows at the inlet were set to 5 and 10 mL min^{-1} during oxidation and reduction, respectively.

4. Conclusions

Using a descriptor-based design principle, we predicted promising redox thermodynamics of the three AA'BO_3-type perovskites $La_{0.5}Ba_{0.5}CoO_{3-\delta}$, $Pr_{0.5}Ba_{0.5}CoO_{3-\delta}$ and $Y_{0.5}Ba_{0.5}CoO_{3-\delta}$. These compounds were further evaluated using dynamic oxygen exchange measurements, with $Y_{0.5}Ba_{0.5}CoO_{3-\delta}$ being identified as most ideal for thermochemical oxygen separation and production. This compound shows the fastest reaction rates, lowest reaction temperatures and highest oxygen exchange capacities compared to those of the tested perovskites in this work, and the state-of-the-art materials $SrCoO_3$ and $SrFeO_3$. The TOS processes was experimentally demonstrated using $Y_{0.5}Ba_{0.5}CoO_{3-\delta}$ and an energy balance indicates that the it could in principle be driven by process waste heat from the solar splitting of CO_2/H_2O. Finally, consecutive redox cycles executed with a packed-bed reactor indicated the potential of both thermochemical oxygen production and separation for scale-up and industrial implementation.

Nomenclature

ca	Cooling air
cg	Cooling gas
cs	Cooling solid
DFT	Density functional theory
E_{el}	Electrical energy (kJ $mol_{O_2}^{-1}$)
E_{th}	Thermal energy (kJ $mol_{O_2}^{-1}$)
$\Delta\bar{g}^{\circ}_{O_2}$	Standard partial molar Gibbs free energy change of metal oxide reduction (kJ $mol_{O_2}^{-1}$)
$\Delta\bar{g}^{\circ *}_{O_2}$	Computed standard partial molar Gibbs free energy change of metal oxide reduction (kJ $mol_{O_2}^{-1}$)
$\Delta\bar{g}^{\circ}_{O_2,\,lim}$	Limiting standard partial molar Gibbs free energy change of metal oxide reduction (kJ $mol_{O_2}^{-1}$)
$\Delta G_V[O]$	Gibbs free energy change of oxygen vacancy formation (eV)
Δh	Enthalpy (kJ $mol_{O_2}^{-1}$)
$\Delta\bar{h}^{\circ}_{O_2}$	Standard partial molar enthalpy change of metal oxide reduction (kJ $mol_{O_2}^{-1}$)
ha	Heating air
hg	Heating gas
hs	Heating solid
LBCO	$La_{0.5}Ba_{0.5}CoO_{3-\delta}$
M_O	Molar mass of O (g mol^{-1})
M_s	Molar mass of reactive sample (g mol^{-1})
m_s	Mass of reactive sample (mg)
L min^{-1}	Standard liter per minute at 298 K and 1 bar
pO_2	Oxygen partial pressure (bar)
$pO_{2,ox,in}$	Oxygen partial pressure at the inlet of the experiment during oxidation (bar)
$pO_{2,ox,out}$	Oxygen partial pressure at the outlet of the experiment during oxidation (bar)
$pO_{2,red,in}$	Oxygen partial pressure at the inlet of the experiment during reduction (bar)
$pO_{2,red,out}$	Oxygen partial pressure at the out let of the experiment during reduction (bar)
p_{tot}	System pressure (bar)
p°	Standard pressure (bar)
PBCO	$Pr_{0.5}Ba_{0.5}CoO_{3-\delta}$
PBR	Packed bed reactor
R	Universal gas constant (J mol_O^{-1} K^{-1})
SEM	Scanning electron microscopy
T_{ox}	Oxidation temperature (K)
$T_{net,eq}$	Net equilibrium temperature (K)
T_{red}	Reduction temperature (K)
TOP	Thermochemical oxygen production
TOS	Thermochemical oxygen separation
TGA	Thermogravimetric analyzer
ΔT	Difference between oxidation and reduction temperatures (K)
XRD	X-ray diffraction
YBCO	$Y_{0.5}Ba_{0.5}CoO_{3-\delta}$
δ	Degree of oxygen nonstoichiometry at thermodynamic equilibrium (–)
δ_{ox}	Degree of oxygen nonstoichiometry after oxidation at thermodynamic equilibrium (–)
δ_{red}	Degree of oxygen nonstoichiometry after reduction at thermodynamic equilibrium (–)
$\Delta\delta$	Oxygen exchange capacity (mol_O $mol_{ABO_3}^{-1}$)

Conflicts of interest

There are no conflicts of interest to declare.

Acknowledgements

We gratefully acknowledge the financial support by the Swiss Competence Center Energy & Mobility, the Helmholtz-Gemeinschaft Deutscher Forschungszentren (Virtuelles Institut SolarSyngas), the European Research Council under the European Union's ERC Advanced Grant (SUNFUELS-No. 320541), and the European Union's Horizon 2020 research and innovation programme (Project SFERA-III – Grant Nr. 823802). The DFT calculations were performed at the High-Performance Computation cluster of ETH Zürich.

References

1 R. M. Thorogood, *Gas Sep. Purif.*, 1991, **5**, 83–94.
2 K. Zhang, J. Sunarso, Z. P. Shao, W. Zhou, C. H. Sun, S. B. Wang and S. M. Liu, *RSC Adv.*, 2011, **1**, 1661–1676.
3 T. Burdyny and H. Struchtrup, *Energy*, 2010, **35**, 1884–1897.
4 A. R. Smith and J. Klosek, *Fuel Process. Technol.*, 2001, **70**, 115–134.
5 P. M. Geffroy, J. Fouletier, N. Richet and T. Chartier, *Chem. Eng. Sci.*, 2013, **87**, 408–433.
6 F. G. Kerry, *Industrial Gas Handbook: Gas Separation and Purification*, CRC Press, 2010.
7 M. Hänchen, A. Stiel, Z. R. Jovanovic and A. Steinfeld, *Ind. Eng. Chem. Res.*, 2012, **51**, 7013–7021.
8 M. Ezbiri, K. M. Allen, M. E. Gàlvez, R. Michalsky and A. Steinfeld, *ChemSusChem*, 2015, **8**, 1966–1971.

9 B. Bulfin, J. Lapp, S. Richter, D. Gubàn, J. Vieten, S. Brendelberger, M. Roeb and C. Sattler, *Chem. Eng. Sci.*, 2019, **203**, 68–75.
10 K. Krishnamurthy, D. Acharya and F. Fitch, *Pilot-Scale Demonstration of a Novel, Low-Cost Oxygen Supply Process and its Integration with Oxy-Fuel Coal-Fired Boilers*, 2008, Tech. rep., Boc Group, Inc., The (A Delaware Corp).
11 B. Moghtaderi, *Energy Fuels*, 2010, **24**, 190–198.
12 J. Vieten, B. Bulfin, F. Call, M. Lange, M. Schmücker, A. Francke, M. Roeb and C. Sattler, *J. Mater. Chem. A*, 2016, **4**(35), 13652–13659.
13 J. Vieten, B. Bulfin, P. Huck, M. Horton, D. Guban, L. Zhu, Y. Lu, K. A. Persson, M. Roeb and C. Sattler, *Energy Environ. Sci.*, 2019, **12**(4), 1369–1384.
14 J. Dou, E. Krzystowczyk, A. Mishra, X. Liu and F. Li, *ACS Sustainable Chem. Eng.*, 2018, **6**(11), 15528–15540.
15 A. M. Narayanan, R. Parasuraman and A. M. Umarji, *Ind. Eng. Chem. Res.*, 2018, **57**(43), 14749–14757.
16 C. L. Muhich, B. W. Evanko, K. C. Weston, P. Lichty, X. H. Liang, J. Martinek, C. B. Musgrave and A. W. Weimer, *Science*, 2013, **341**, 540–542.
17 L. J. Venstrom, R. M. De Smith, Y. Hao, S. M. Haile and J. H. Davidson, *Energy Fuels*, 2014, **28**, 2732–2742.
18 W. Villasmil, M. Brkic, D. Wuillemin, A. Meier and A. Steinfeld, *J. Sol. Energy Eng.*, 2014, **136**, 011016.
19 J. Enkovaara, C. Rostgaard, J. J. Mortensen, J. Chen, M. Dulak, L. Ferrighi, J. Gavnholt, C. Glinsvad, V. Haikola, H. A. Hansen, H. H. Kristoffersen, M. Kuisma, A. H. Larsen, L. Lehtovaara, M. Ljungberg, O. Lopez-Acevedo, P. G. Moses, J. Ojanen, T. Olsen, V. Petzold, N. A. Romero, J. Stausholm-Moller, M. Strange, G. A. Tritsaris, M. Vanin, M. Walter, B. Hammer, H. Hakkinen, G. K. H. Madsen, R. M. Nieminen, J. Nørskov, M. Puska, T. T. Rantala, J. Schiotz, K. S. Thygesen and K. W. Jacobsen, *J. Phys.: Condens. Matter*, 2010, **22**, 253202.
20 J. J. Mortensen, L. B. Hansen and K. W. Jacobsen, *Phys. Rev. B: Condens. Matter Mater. Phys.*, 2005, **71**, 035109.
21 S. R. Bahn and K. W. Jacobsen, *Comput. Sci. Eng.*, 2002, **4**, 56–66.
22 B. Hammer, L. B. Hansen and J. K. Nørskov, *Phys. Rev. B: Condens. Matter Mater. Phys.*, 1999, **59**, 7413–7421.
23 A. J. Medford, J. Wellendorff, A. Vojvodic, F. Studt, F. Abild-Pedersen, K. W. Jacobsen, T. Bligaard and J. K. Norskov, *Science*, 2014, **345**, 197–200.
24 M. García-Mota, A. Vojvodic, H. Metiu, I. C. Man, H. Y. Su, J. Rossmeisl and J. K. Nørskov, *ChemCatChem*, 2011, **3**, 1607–1611.
25 M. Ezbiri, M. Takacs, B. Stolz, J. Lungthok, A. Steinfeld and R. Michalsky, *J. Mater. Chem. A*, 2017, **5**(29), 15105–15115.
26 R. Michalsky, V. Botu, C. M. Hargus, A. A. Peterson and A. Steinfeld, *Adv. Energy Mater.*, 2014, **4**, 1401082.
27 I. Barin, *Thermochemical Data of Pure Substances*, 1993.
28 J. R. Scheffe and A. Steinfeld, *Energy Fuels*, 2012, **26**, 1928–1936.
29 L. B. Pankratz, *Thermodynamic Properties of Elements and Oxides*, USA, 1982.
30 R. Michalsky, D. Neuhaus and A. Steinfeld, *Energy Technol.*, 2015, **3**, 784–789.
31 I. O. Troyanchuk, N. V. Kasper, D. D. Khalyavin, H. Szymczak, R. Szymczak and M. Baran, *Phys. Rev. B: Condens. Matter Mater. Phys.*, 1998, **58**, 2418–2421.
32 T. Nakajima, M. Ichihara and Y. Ueda, *J. Phys. Soc. Jpn.*, 2005, **74**, 1572–1577.
33 M. M. Seikh, V. Pralong, O. I. Lebedev, V. Caignaert and B. Raveau, *J. Appl. Phys.*, 2013, **114**, 013902.
34 T. Vogt, P. M. Woodward, P. Karen, B. A. Hunter, P. Henning and A. R. Moodenbaugh, *Phys. Rev. Lett.*, 2000, **84**, 2969–2972.
35 S. M. Babiniec, E. N. Coker, J. E. Miller and A. Ambrosini, *Sol. Energy*, 2015, **118**, 451–459.
36 M. Takacs, M. Hoes, M. Caduff, T. Cooper, J. R. Scheffe and A. Steinfeld, *Acta Mater.*, 2016, 700–710.
37 W. G. Mallard and P. J. Linstrom, *webbook.nist.gov, retrieved February 2016)*, Gaithersburg MD, 1998.
38 D. Marxer, P. Furler, J. Scheffe, H. Geerlings, C. Falter, V. Batteiger, A. Sizmann and A. Steinfeld, *Energy Fuels*, 2015, **29**, 3241–3250.
39 J. H. Jeong, L. S. Kim, J. K. Lee, M. Y. Ha, K. S. Kim and Y. C. Ahn, presented in part at the ASEM Turbo Expo 2007: Power for land, sea and air, 2007.
40 W. Zhou, C. T. Lin and W. Y. Liang, *Adv. Mater.*, 1993, **5**, 735–738.
41 J. Bugge, S. Kjaer and R. Blum, *Energy*, 2006, **31**, 1437–1445.